UMYU Scientifica, Vol. 4 NO. 3, September 2025, Pp 381 – 399
https://doi.org/10.56919/usci.2543.038
ISSN: 2955 – 1145 (print); 2955 – 1153 (online)
A periodical of the Faculty of Natural and Applied Sciences, UMYU, Katsina

ORIGINAL RESEARCH ARTICLE

Watermelon Rind-Based Adsorbent for *Eriochrome Black T* Removal: Synergistic Experimental and DFT Analysis

Abosede Adejoke Badeji[1]*, Abimbola Aina Ogundiran[1]*, Mosunmola Iretomiwa Sanni[1], Segun D. Oladipo[2] and Adejoke Deborah Osinubi[1]

[1]Department of Chemical Sciences, Tai Solarin Federal University of Education, Ijagun, Ogun State, Nigeria
[2]Department of Chemical Sciences, Olabisi Onabanjo University, P.M.B 2002, Ago-Iwoye, Nigeria

ABSTRACT

The removal of synthetic dyes from wastewater remains a major environmental challenge due to their toxicity, persistence, and resistance to traditional treatment methods. This study explores the potential of alkaline-treated watermelon rind (WR), a low-cost, eco-friendly adsorbent, to remove the azo dye *Eriochrome Black T* (EBT) from aqueous solution via experimental and Density Functional Theory (DFT) studies. A series of batch adsorption experiments was performed, and the optimal EBT removal (78%) was obtained at pH 2, an adsorbent dosage of 0.8 g, an initial concentration of 30 mg/L, a contact time of 50 minutes, and a temperature of 50 °C. FTIR spectra confirmed that functional groups, including N-H, C-H, C=O, and aromatic C–H in the WR surface, played a key role in dye binding. The adsorption kinetics best matched the pseudo-second-order model (R^2 = 0.99), indicating chemisorption and monolayer coverage. Thermodynamic analysis ($\Delta G° = -6.25$ kJ mol^{-1}, positive $\Delta H°$ and $\Delta S°$) showed that the process is feasible, spontaneous, and endothermic. The equilibrium data fitted best to the Freundlich isotherm (R^2 = 0.998), suggesting a multilayer adsorption process on a heterogeneous surface. Complementary DFT studies provided insight into the electronic properties and reactivity of the EBT conformers, with EBT-5 having the lowest energy gap (ΔE = 1.43 eV), suggesting the highest reactivity towards WR. Molecular electrostatic potential surface maps supported these findings, highlighting potential active adsorption sites. Together, the experimental and computational findings demonstrate that alkaline-modified WR is an efficient, sustainable material for the removal of EBT dyes from wastewater and provide insight into the underlying adsorption mechanisms.

ARTICLE HISTORY

Received June 11, 2025
Accepted September 18, 2025
Published September 30, 2025

KEYWORDS

Adsorption isotherm, Eriochrome Black T dye, Watermelon rind, Wastewater treatment, DFT, Kinetics

INTRODUCTION

Water pollution continues to pose a significant global threat, especially in densely populated areas where industrial activities are concentrated (Kishor et al., 2020, 2021; Lellis et al., 2019). A primary contributor to this issue is the discharge of untreated effluents from textile manufacturing, which are heavily laden with synthetic dyes (Kishor et al., 2020). These dyes are known for their toxicity, resistance to degradation, and long-term persistence in the environment, all of which endanger both aquatic ecosystems and terrestrial life (Kishor et al., 2020; Vlahović et al., 2024).

Dyes are complex synthetic chemicals commonly used to color textiles, paper, leather, and plastics (Padhi, 2012). Their aromatic frameworks and synthetic composition render them particularly resistant to natural biodegradation (Padhi, 2012). One such dye, *Eriochrome Black* T (EBT), an anionic compound frequently employed in analytical applications such as complexometric titrations, has also been linked to environmental hazards, including toxicity and potential mutagenicity (Yaseen & Scholz, 2019). Once present in aquatic environments, dyes such as EBT limit light penetration, disrupting photosynthesis in aquatic plants and destabilizing ecosystems (Yaseen & Scholz, 2019). These pollutants can bioaccumulate through the food web, ultimately posing carcinogenic risks to human health with prolonged exposure or ingestion of contaminated water (Yaseen & Scholz, 2019).

To address dye pollution, a range of chemical and physical treatment methods, such as coagulation, chlorination, filtration, and membrane separation, have been applied. However, many of these technologies are cost-prohibitive, energy-demanding, or inadequate for large-scale implementation (Thakur & Chauhan, 2018; Yaseen &

Correspondence: Abosede Adejoke Badeji. Department of Chemical Sciences, Tai Solarin Federal University of Education, Ijagun, Ogun State, Nigeria. ✉ ogunlanaaa@tasued.edu.ng.

How to cite: Badeji, A. A., Ogundiran, A. A., Sanni, M. I., Oladipo, S. D. & Osinubi, A. D. (2025). Watermelon Rind-Based Adsorbent for *Eriochrome Black T* Removal: Synergistic Experimental and DFT Analysis. *UMYU Scientifica*, 4(3), 381 – 399. https://doi.org/10.56919/usci.2543.038

Scholz, 2019). In contrast, adsorption has gained prominence as an effective, low-cost method for dye removal from wastewater (Said et al., 2021). This technique stands out for its straightforward design, ease of operation, and capability to produce high-quality treated water (Yaseen & Scholz, 2019). Additionally, adsorption is versatile, working well across a broad range of organic pollutants, making it particularly suited for industrial wastewater applications (Yaseen & Scholz, 2019).

Recent efforts have increasingly focused on identifying sustainable, cost-effective adsorbents derived from agricultural waste materials (Afolalu et al., 2022; Johnson et al., 2008; Liu et al., 2024; Priyan et al., 2024). Among these, watermelon rind has emerged as a promising candidate due to its high content of cellulose, hemicellulose, lignin, and pectin (Akinyemi et al., 2020; Othman et al., 2016). Accounting for nearly 30% of the fruit's weight, the rind is often discarded as waste following consumption (Beegum et al., 2024). However, studies have demonstrated its potential as a biosorbent for various pollutants, including synthetic dyes (Onyango et al., 2025; Rekha Krishnan et al., 2023; Wang et al., 2022). The natural abundance of functional groups in cellulose and lignin enables effective interactions with dye molecules during the adsorption process (Shukla et al., 2024). Alkaline treatment of the rind further enhances this capacity by increasing surface area and introducing more active binding sites. This involves treating the rind with an alkaline solution that removes residual impurities and activates the surface for greater dye uptake (Onyango et al., 2025). The resulting material is plentiful, biodegradable, and offers a viable, sustainable solution for industrial wastewater treatment (Onyango et al., 2025).

While experimental studies provide macroscopic insights into adsorption performance, they provide inadequate information on the microscopic interactions governing adsorbate-adsorbent binding. Computational studies, in particular density functional theory (DFT) calculations, have emerged as a powerful tool to bridge this gap by providing information on the electronic properties, molecular orbitals, charge distributions, reactivity, and reactive sites of both the adsorbent and the dye molecules (Anadebe et al., 2025). The combined experimental and adsorption studies with DFT computations is a powerful technique to unveil adsorption mechanisms, validate experimental observations, and understand the processes governing adsorption at the molecular level (Anadebe et al., 2025). However, only a few of these studies integrated experimental and DFT approaches to analyze agro-waste adsorbents for azo-dye removal. This study therefore, presents a combined experimental and computational investigation of the potential of alkaline-modified watermelon rind as an efficient, eco-friendly adsorbent for removing EBT dye from wastewater. The adsorption process was evaluated via kinetic, isotherm, and thermodynamic studies to understand the mechanism, adsorption capacity, and spontaneity. More so, the integrated DFT studies will reveal the electronic properties and molecular interactions between the dye and the key functional groups of the WR. The synergy between these two methods will provide robust insights into adsorption behavior, guiding the development of cost-effective, sustainable materials for dye remediation in wastewater treatment.

MATERIALS AND METHODS

Preparation and Modification of Adsorbent

Watermelon rinds (WR) used in this work were sourced from the New Market area in Ijebu-Ode, Nigeria. After collection, the rinds were rinsed with tap water to remove surface debris, then thoroughly washed with distilled water to remove any residual impurities. The cleaned rinds were then left to air-dry under direct sunlight for seven days. Once thoroughly dried, the rinds were ground into smaller particles using an electric blender. To activate the adsorbent, the crushed material was soaked in 0.1 M NaOH for 24 hours, a chemical treatment designed to enhance adsorption efficiency by increasing surface area and clearing blocked active sites. The modified rinds were then filtered and oven-dried at 80°C to eliminate moisture. Finally, the dried samples were ground once more and passed through a 30-mesh sieve to ensure uniform particle size. The fine powder was stored in sealed plastic bags for later use in the adsorption experiments.

Preparation of Adsorbate: *Eriochrome Black T* Dye Solution

To prepare the adsorbate, a stock solution of EBT dye was formulated by dissolving 0.25 g of the dye in 500 mL of distilled water, yielding a concentration of 500 ppm. From this stock, working solutions at 10 ppm, 20 ppm, and 30 ppm were prepared by serial dilution. These standard solutions served as the adsorbates in the batch adsorption experiments.

Characterization of Adsorbent

The surface chemistry of the alkaline-modified watermelon rind (WR) adsorbent was characterized using Fourier Transform Infrared (FTIR) spectroscopy to identify its functional groups. For this, WR samples were loaded onto potassium bromide (KBr) discs and then examined using an FTIR spectrophotometer. The resulting spectra provided valuable information on the chemical bonds and surface functionalities involved in the adsorption process, and were recorded over 4000–400 cm^{-1} with a resolution of 4 cm^{-1}.

Batch Adsorption Studies

To assess the performance of WR as an adsorbent for EBT dye removal, batch adsorption experiments were performed. Each test was conducted in a 250 mL Erlenmeyer flask containing 25 mL of the dye solution. These flasks were placed in a temperature-controlled water bath shaker and agitated at 160 rpm for 30 minutes to reach equilibrium conditions.

In every experiment, one parameter, such as pH, concentration, or dosage, was systematically varied while the others were kept constant to determine the optimal adsorption conditions. The variables examined included the pH of the solution (ranging from 2 to 10), adsorbent dosage (0.1 to 1.0 g), initial dye concentration (5 to 30 mg/L), contact time (5 to 60 minutes), and temperature (25 to 60°C). The pH of the solution is adjusted using 0.1M of HCl/NaOH. After equilibrium was reached, the solutions were centrifuged to separate the adsorbent from the dye. The residual dye concentration in the supernatant was measured using a UV-Vis spectrophotometer (Hitachi U-3210, Japan) at the maximum absorbance wavelength (λmax). All results obtained are in triplicate. The means values were obtained for further computations.

Data Analysis

All adsorption experiments were conducted in triplicate (n = 3), and the mean values were used for analysis. Error bars in Figures 3–6 represent the standard deviation of triplicate runs. The adsorption data obtained from the UV-Vis spectrophotometer were used to calculate the removal efficiency (%) and adsorption capacity q_e in mg/g of the watermelon rind for the removal of EBT dye using equations (1) and (2) below.

Dye Removal Rate (%): $\frac{C_i - C_e}{C_i} \times 100$ (1)

Adsorption Capacity q_e (mg/g): $\frac{C_i - C_e}{m} \times V$ (2)

Where: C_i is the C_e are the initial and equilibrium dye concentration (mg/L) respectively, V is the solution volume (L), and m is the adsorbent mass (g)

Adsorption Kinetic Studies

The Pseudo-First-Order kinetic Model can analyze the adsorption kinetic mechanism. The pseudo-first-order model (Lagergren, 1898) assumes physical adsorption as the rate-limiting step. Its linear form is represented in equation (3) below

$$\log(q_e - q_t) = \log q_e - (\frac{K_1}{2.303})t \quad (3)$$

where q_t (mg/g) is the adsorption capacity at time t (min), and k_1 is the first-order rate constant (min^{-1}).

The Pseudo-second-order model (Ho & McKay, 1999) presumes chemisorption as the dominant mechanism. The linear equation for the plot of $\frac{t}{q_t}$ vs t is represented in equation (4) below

$$\frac{t}{q_t} = \frac{1}{k_2 q_e^2} + \left(\frac{1}{q_e}\right)t \quad (4)$$

Where k_2 is the second-order rate constant (g/mg)

Thermodynamic Studies

Thermodynamic parameters, including the Gibbs free energy change (ΔG), enthalpy change (ΔH), and entropy change (ΔS) for the adsorption process, were derived from temperature-dependent Langmuir constants (K_L) at 298, 308, and 318 K to determine the adsorption feasibility and the thermodynamic nature of the process involved. The van't Hoff equations (5-7) below were used

$$\ln K_L = \frac{\Delta S}{R} - \frac{\Delta H}{R} \cdot \frac{1}{T} \quad (5)$$

$$K_L = \frac{C_{Ae}}{C_e} \quad (6)$$

$$\Delta G = -RT ln\, K_L \quad (7)$$

where ΔG (kJ/mol), ΔH (kJ/mol), and ΔS (kJ/mol·K) are Gibbs free energy, enthalpy, and entropy changes, respectively. R (8.314 J/mol·K) is the gas constant, T (K) is the temperature, and K_L is the Langmuir constant. ΔH and ΔS were obtained from the slope and intercept of $\ln K_L$ vs. $\frac{1}{T}$.

Equilibrium Adsorption Isotherm Models

The adsorption isotherms were used to evaluate the equilibrium adsorption. The Langmuir isotherm model (Langmuir, 1918) describes monolayer adsorption on a homogeneous surface with a finite number of identical active sites. The linearized form of the model is expressed in equation (8) below

$$\frac{1}{q_e} = \frac{1}{q_m K_L C_e} + \frac{1}{q_m} \quad (8)$$

where q_e (mg/g) and C_e (mg/L) represent the equilibrium adsorption capacity and residual dye concentration, respectively. K_L (L/mg) is the Langmuir equilibrium constant, and q_m (mg/g) represents the maximum monolayer adsorption capacity.

The feasibility of adsorption is assessed using the dimensionless separation factor (R_L) according to equation (9)

$$R_L = \frac{1}{1 + K_L C_0} \quad (9)$$

where C_0 (mg/L) is the initial dye concentration. Adsorption is favorable if $0 < R_L < 1$, unfavorable if $R_L > 1$ and irreversible if $R_L = 0$ (Harrache & Abbas, 2022).

The Freundlich model (Freundlich, 1906) applies to heterogeneous surfaces with non-uniform adsorption energies. Its linearized form is expressed in equation (10) below

$$\ln q_e = \frac{1}{n} lnC_e + lnK_F \quad (10)$$

where, K_F (L/g) reflects adsorption capacity, and $1/n$ (dimensionless) indicates adsorption intensity. A value of $1/n$ <1 suggests favorable adsorption. The plot of $\ln q_e$ as a function of $\ln C_e$ provides a straight line with $1/n$ as the slope and lnK_F as the intercept.

Computational Details

Quantum chemical calculations were conducted using the Gaussian 16 software suite, employing Density Functional Theory (DFT) as the computational framework (Frisch et al., 2016). The molecular geometries of various EBT conformers were optimized using the B3LYP functional, a hybrid approach that integrates Becke's three-parameter exchange with the Lee–Yang–Parr correlation functional (Becke, 1993; Hassan, 2014). Calculations were carried out with the 6-311++G(2d,p) basis set, which includes both diffuse and polarization functions. This extended basis set improves the accuracy of electronic structure predictions, especially in valence and peripheral electron regions, and is particularly suited for capturing subtle intermolecular interactions (Andersson & Uvdal, 2005). Frequency analyses at the same theoretical level confirmed that the optimized geometries represent true minima on the potential energy surface (Grandhi, 1993). The 3D molecular structures were visualized using CYLview software (Legault, 2016), while Chemcraft (Andrienko, 2010) was used to display molecular orbitals and optimized geometries. GaussView 6.0 supported input setup, output interpretation, and the visualization of electrostatic potential surfaces and Natural Bond Orbital (NBO) interactions (Dennington et al., 2023).

To explore electrostatic behavior, a Molecular Electrostatic Potential (MESP) map was generated. This map uses a color gradient to differentiate regions of electrostatic potential: blue zones indicate areas of positive potential suitable for nucleophilic attack, red zones mark negative regions conducive to electrophilic interactions, and green denotes neutral charge areas (Suresh et al., 2022).

Frontier Molecular Orbital (FMO) analysis was performed using the B3LYP/6-311++G(2d,p) level to assess electronic characteristics (Huang et al., 2017). Energies of the Highest Occupied Molecular Orbital (HOMO) and Lowest Unoccupied Molecular Orbital (LUMO) were calculated, and the resulting HOMO-LUMO energy gap (ΔEg) provided insight into electron excitation behavior. The HOMO level correlates with the molecule's ionization potential, while the LUMO relates to its electron affinity (Badeji et al., 2024). The HOMO-LUMO gap reflects the energy required for an electronic transition and serves as a key indicator of intramolecular charge-transfer capabilities (Aihara, 1999). Smaller gaps typically imply higher chemical reactivity and lower kinetic stability, as electron redistribution is easier (Oladipo et al., 2023). Additionally, quantum chemical reactivity descriptors were derived to further interpret the molecular behavior (Aihara, 1999; Huang et al., 2017; Islam & Ghosh, 2011; Ogunlana et al., 2018; Zhan et al., 2003). These included chemical hardness (η), which indicates resistance to electron transfer, and softness (σ), its inverse, representing how readily the molecule accommodates changes in electron density. Electronegativity (χ), estimated as the mean of HOMO and LUMO energies, quantifies the molecule's tendency to attract electrons. The electrophilicity index (ω) was computed to assess the molecule's reactivity toward nucleophilic species (Pal & Chattaraj, 2023). These descriptors collectively provide insights into EBT's stability and interaction mechanisms and were computed using the equations reported in the literature.

The workflow diagram for the synergistic integration of experimental adsorption studies and DFT-based computational analysis is shown in Figure 1 below.

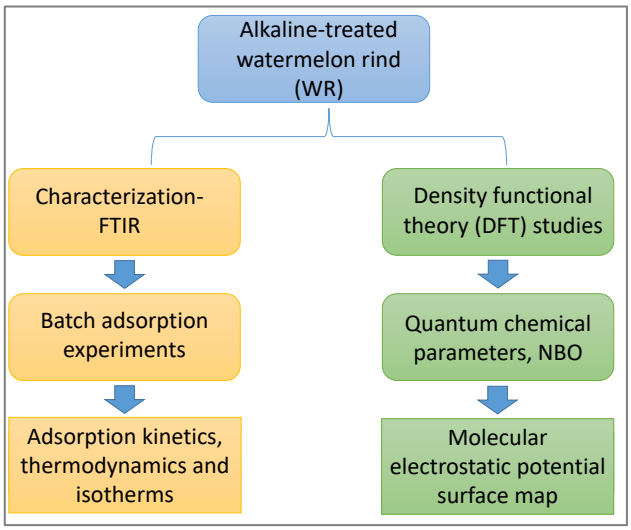

Figure 1: Workflow diagram of the experimental and computational phases for the adsorption of EBT dye on WR.

RESULTS AND DISCUSSION

Characterization of the adsorbent

FTIR analysis is crucial for identifying functional groups responsible for dye adsorption on adsorbent surfaces. As illustrated in Figure 2, the FTIR spectra of watermelon rind before and after exposure to *Eriochrome Black T* dye reveal several significant functional groups. A broad absorption band observed between 3600 and 3000 cm^{-1} corresponds to N–H stretching vibrations typical of N-substituted amides. The peak at 2850 cm^{-1} is attributed to C–H stretching in aldehydes, while the strong absorption at 1739 cm^{-1} signifies C=O stretching associated with ketones, esters, lactones, quinones, or carboxylic acids. Additionally, aromatic C–H bending vibrations are evident in the 800 to 400 cm^{-1} range (Olukanni & Mnenga, 2015). The observed shifts in peak positions after dye uptake indicate the active participation of carbonyl groups, amides, and aromatic rings in the adsorption mechanism.

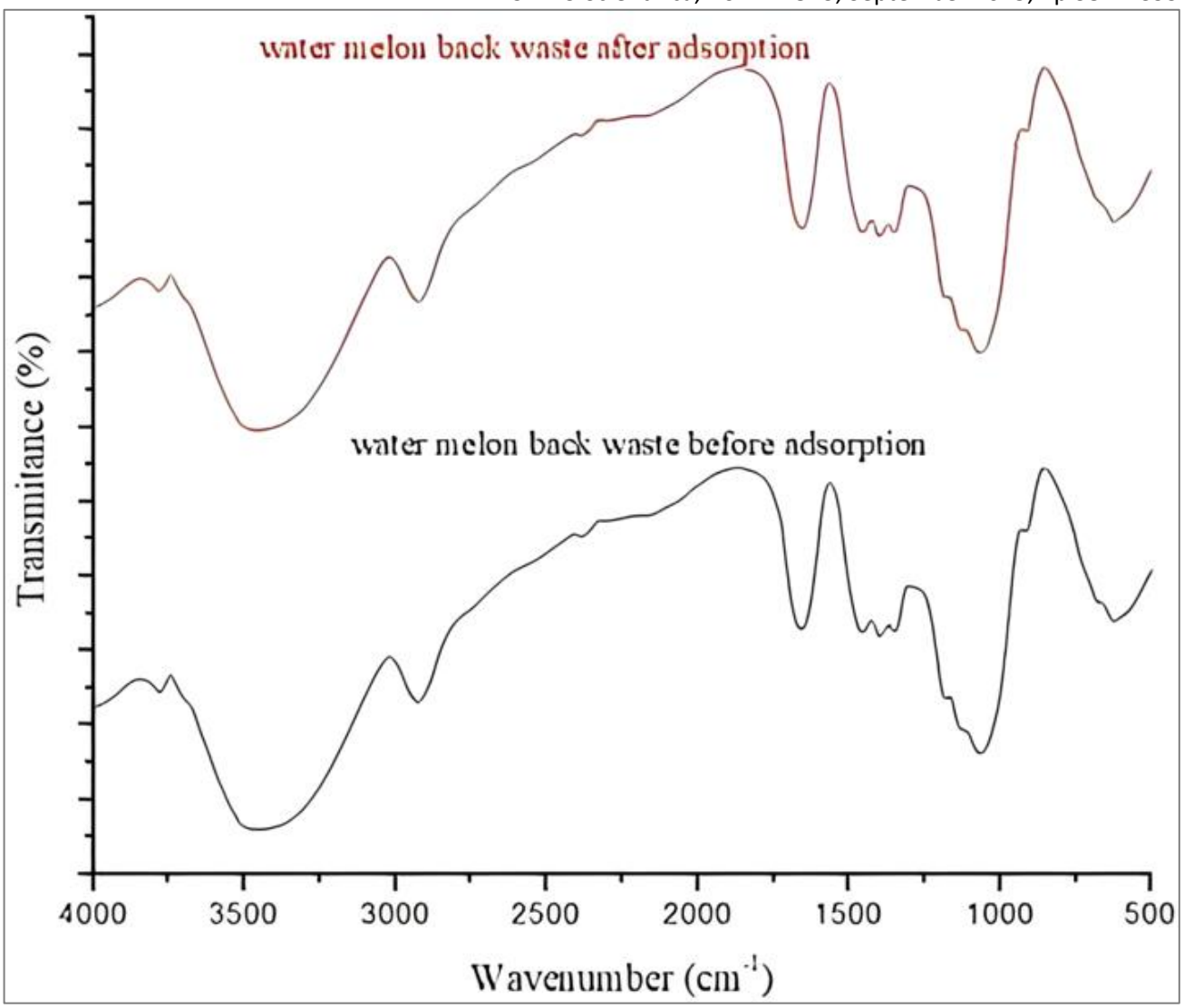

Figure 2: FTIR Spectrum of Watermelon rind before and after adsorption of EBT Dye

Effect of Different Parameters on the Adsorption of EBT Dye on Watermelon Rind

Effect of pH

The pH of the solution is a critical factor influencing the adsorption efficiency, as initial pH conditions significantly affect the interaction between the adsorbent and the adsorbate (Al-Degs et al., 2008). As shown in Figure 3, adsorption capacity declines with increasing pH, with a maximum efficiency of 78% recorded at pH 2 and a minimum of 49% at pH 8. At lower pH levels, the abundance of hydrogen ions enhances the surface positivity of the adsorbent, thereby promoting electrostatic attraction with the negatively charged dye molecules. In contrast, elevated pH values diminish adsorption efficiency due to increased charge repulsion, a phenomenon commonly reported in adsorption mechanism studies (Fujimoto et al., 2017).

Effect of Adsorbent Dosage

As shown in Figure 4, adsorption efficiency increased markedly with a rise in adsorbent dosage from 0.1 g to 0.8 g, reaching a peak removal rate of 76% before declining slightly at 1.0 g. This behavior is primarily linked to the expanded surface area and the greater number of available adsorption sites as more adsorbent is introduced (Foster, 2015). Initially, the enhancement in dye removal corresponds to the increased availability of active binding sites. However, beyond a certain dosage, further increases offer minimal benefit, and the efficiency begins to drop. This reduction at higher dosages is likely due to an unfavorable dye-to-biosorbent ratio, which limits effective interaction between dye molecules and the adsorbent surface (Foster, 2015).

Effect of Temperature

As illustrated in Figure 5, the adsorption capacity of EBT dye increased with temperature, peaking at 50 °C before declining at higher temperatures. This pattern indicates that the adsorption process is endothermic, where elevated temperatures initially promote stronger molecular interactions. However, beyond the optimal point, the decline in efficiency is likely due to a reduction in available surface area or weakened intermolecular forces at elevated thermal conditions. These findings are consistent with those by Mahmoodi and co-workers, who observed

similar thermal effects on dye adsorption (Mahmoodi, 2011).

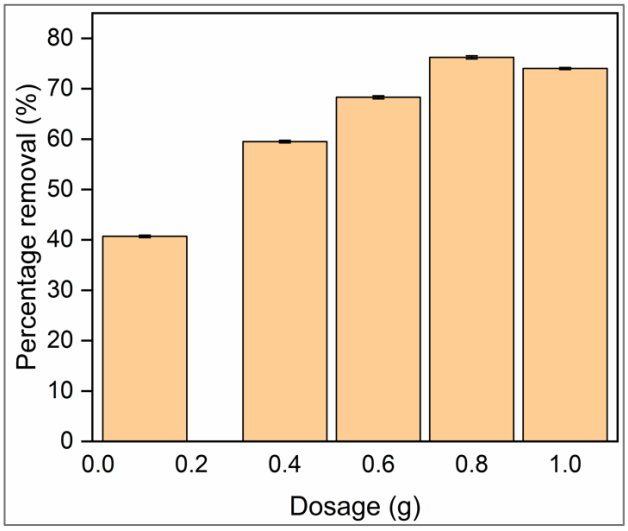

Figure 4: Effect of adsorbent dosage on the adsorption of *Eriochrome Black T* dye using watermelon rind with standard deviation error bars at optimum conditions (pH 2, temperature at 25° C, 120 minutes contact time, concentration at 30ppm).

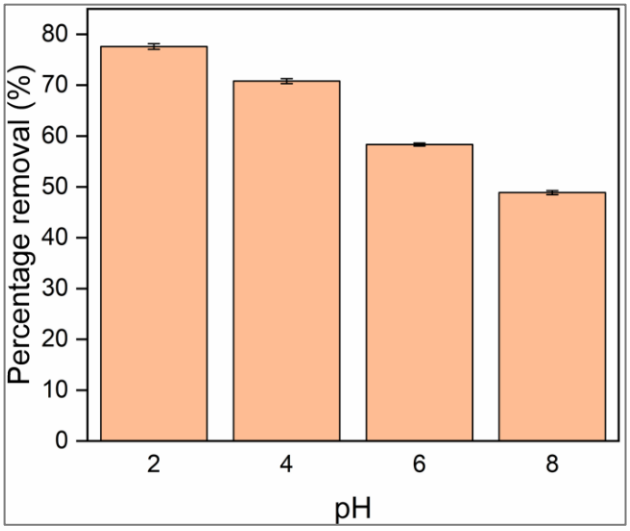

Figure 3: Effect of solution pH on the adsorption of EBT dye using watermelon rind with standard deviation error bars at optimum conditions (0.8g dosage, temperature at 25° C, 120 minutes contact time, concentration at 30ppm).

Effect of Contact Time and Initial Concentration

The adsorption rate increased steadily with time and the initial EBT dye concentration. For dye concentrations ranging from 5 ppm to 30 ppm, adsorption rates plateaued after 35 minutes and showed a slight decline beyond 45 minutes (Figure 6). Higher adsorbate concentrations increase competition for binding sites, consistent with findings by Okeimen and co-workers (Okieimen et al., 2007). This trend is attributed to the increase in mass transfer driving force, which enhances EBT adsorption. Additionally, the amount of dye removed rose with increasing initial dye concentration, reinforcing the role of contact time in adsorption efficiency. The removal of EBT was notably influenced by the duration of interaction within a defined time frame.

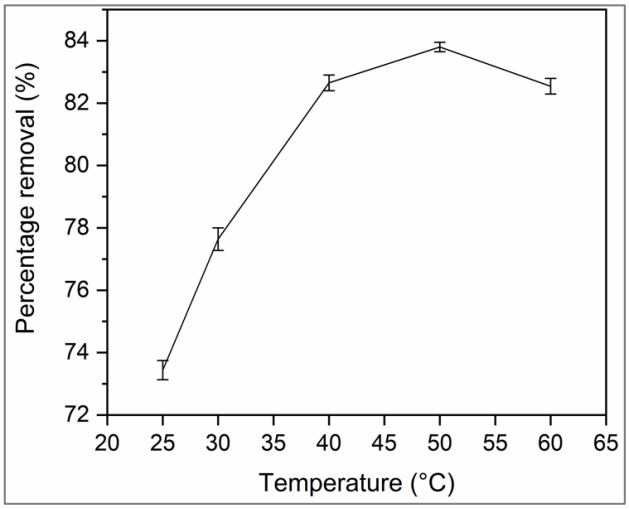

Figure 5: Effect of temperature on the adsorption of *Eriochrome Black T* dye using watermelon rind with standard deviation error bars at optimum conditions (pH 2, dosage at 0.8g, at 120 minutes contact time, concentration at 30ppm).

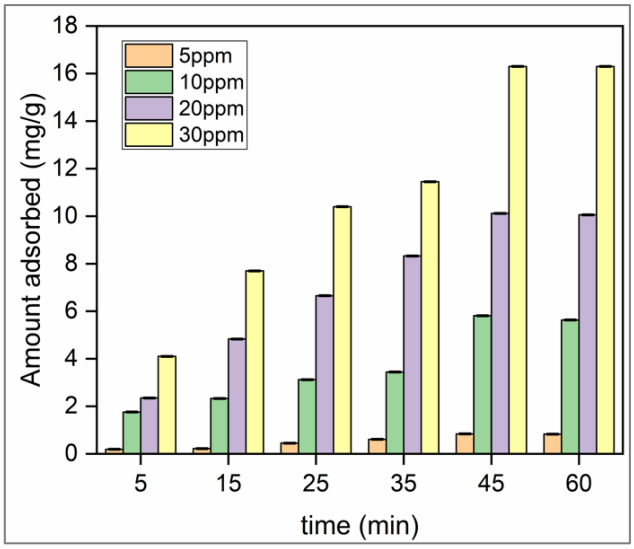

Figure 6: Effect of contact time and initial dye concentration on the adsorption of *Eriochrome Black T* dye using watermelon rind with standard deviation error bars at optimum conditions (pH 2, temperature at 25° C, 0.8g dosage, and concentration at 30ppm).

Thermodynamic Studies

The thermodynamic parameters validate that the adsorption process is spontaneous and endothermic. The Van't Hoff plot (lnK vs. 1/T) reveals a positive ΔH°, confirming the endothermic nature of the process, while a positive ΔS° indicates increased randomness at the solid-liquid interface. Additionally, the negative ΔG° suggests the feasibility of adsorption, reinforcing its spontaneity (Figure 7). A detailed summary of these thermodynamic parameters is provided in Table 1.

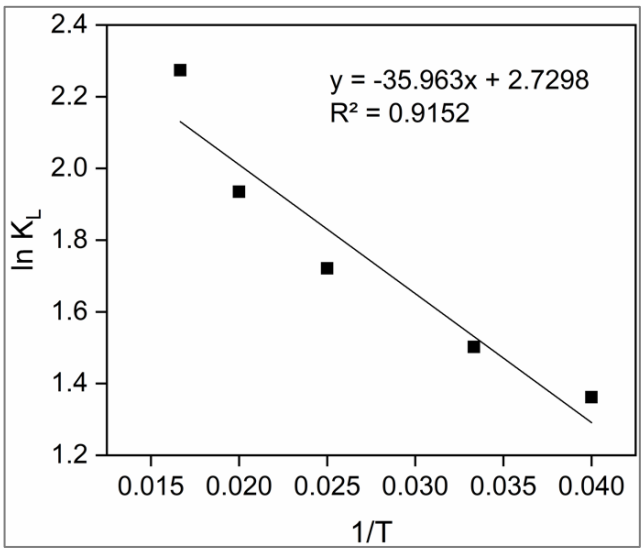

Figure 7: Plot of $\ln K_L$ vs 1/T for the removal of EBT dye onto watermelon rind as an adsorbent

Adsorption Kinetics

The experimental adsorption data were analyzed using pseudo-first-order and pseudo-second-order kinetic models (Figure 8a and 8b). The parameters derived from these models, along with their respective correlation coefficients (R^2), are summarized in Table 2. Based on the correlation coefficient $R^2 = 0.993$, the adsorption of EBT dye aligns well with the pseudo-second-order model, indicating a strong fit (Figure 8b). Furthermore, the equilibrium concentration (q_e) obtained from this model closely matches the experimentally determined q_e value, reinforcing the reliability of the kinetic analysis.

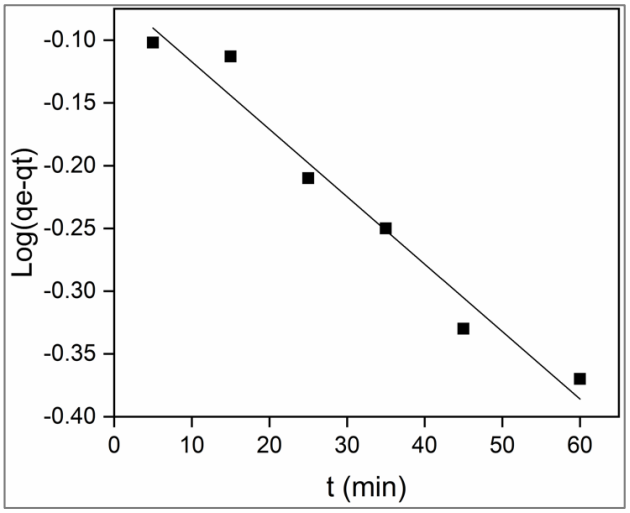

Figure 8a: Pseudo-first-order kinetic model for the adsorption of EBT dye using watermelon rind.

Isotherm Studies

Adsorption isotherms elucidate the interactions between adsorbates and adsorbents. In this study, both the Langmuir and the Freundlich models were employed to fit the experimental data, with the Freundlich isotherm emerging as the superior model (Figure 9a and 9b). As detailed in Table 3, all calculated isotherm constants, including correlation coefficients (R^2) reaching 0.99, demonstrate that the Freundlich model consistently provides a better fit across all tested temperatures compared to the Langmuir isotherm. This model accounts for the heterogeneous distribution of active sites and interactions among adsorbed molecules, thereby providing an accurate description of adsorption behavior. Consequently, the Freundlich isotherm model most effectively represents the experimental data for the adsorbent's removal of EBT, in agreement with the findings of Vigdorowitsch and co-workers (Vigdorowitsch et al., 2021).

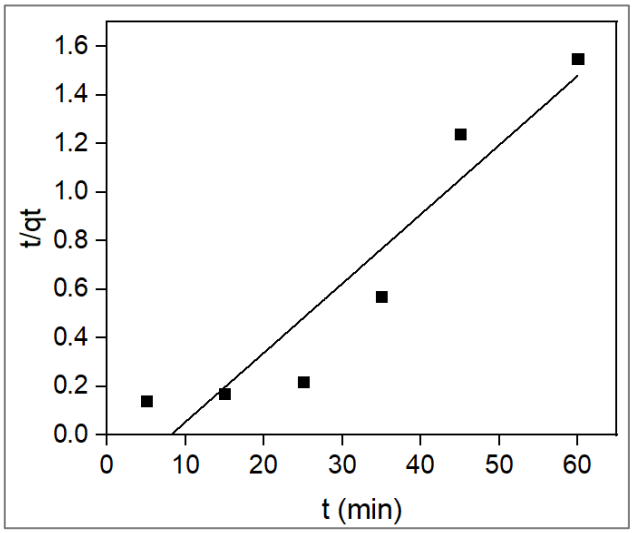

Figure 8b: Pseudo-second-order kinetic model for the adsorption of EBT dye using watermelon rind.

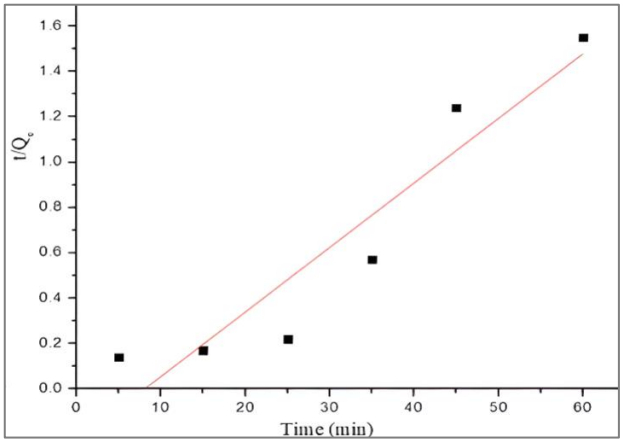

Figure 9a: Langmuir adsorption isotherm model for *Eriochrome Black T* dye using watermelon rind.

When benchmarked against recent bio-adsorbent studies, the adsorption capacity of the present system ($Q_{max} \approx$ 16.30 mg/g; 78 % efficiency, $\Delta G° = -4.43$ KJ/mol) to remove EBT dye is lower than those reported for nickel modified orange peel ($Q_{max} \approx$ 71.42 mg/g, 98 % efficiency, $\Delta G° = -4.46$ KJ/mol), rice hull-based activated carbon (93.14 %), green coffee residue (≈100%), acid-treated tea waste (95%), and rice husk (94%) under optimized conditions (Table 4). The reason for this difference appears to be primarily due to differences in

Table 1: Thermodynamic parameters for the sorption of EBT dye using watermelon rind.

T (^{O}C)	ΔG (kJ/mol)	ΔH (kJ/mol)	ΔS (kJ/mol)
25	-2.25		
30	-3.83		
40	-4.43	23.17	11.63
50	-5.33		
60	-6.25		

Table 2: Comparison of pseudo-first-order and pseudo-second-order adsorption rate constants.

		PSUEDO FIRST- ORDER					PSUEDO SECOND- ORDER			
	C_e	Q_e(exp) (mg/g)	Q_e(cal) (mg/g)	K_1 (min^{-1})	R^2	% SSE	Qe (cal)	K_2	R^2	% SSE
5	2.66	0.83	1.44	0.02	0.95	0.22	0.96	0.13	0.99	0.05
10	4.32	5.63	3.47	0.02	0.96	0.12	4.89	0.13	0.99	0.04
20	7.48	10.06	7.33	0.03	0.99	0.08	9.13	0.15	0.99	0.03
30	9.56	16.3	10.14	0.05	0.89	0.11	16.12	0.24	0.99	0
35	11.22	18.24	14.27	0.05	0.94	0.05	17.65	0.36	0.99	0.01

surface chemistry, porosity, and treatment process among these adsorbents. Adsorbents such as acid-treated tea waste and green coffee residues both contain abundant oxygen-containing functionalities (–COOH, –OH, –C=O), which provide electrostatic attraction and hydrogen bonding between the anionic EBT dye and the adsorbent. On the other hand, untreated watermelon rinds are primarily lignocellulosic, providing numerous potential binding sites; however, few of these sites may be active due to minimal surface modification.

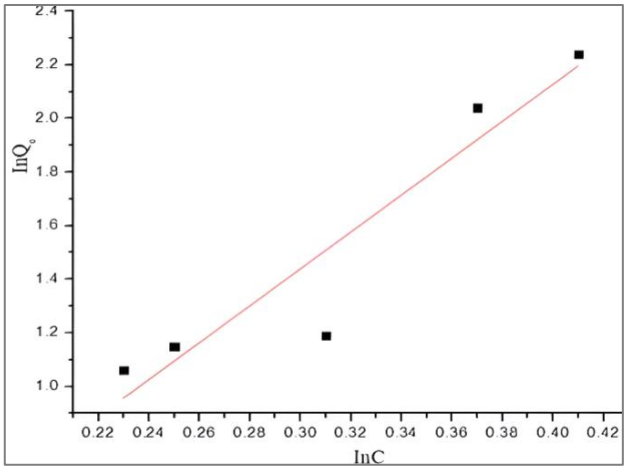

Figure 9b: Freundlich adsorption isotherm model for *Eriochrome Black T* dye using watermelon rind.

Also, many of the adsorbents reported in Table 4 have undergone various chemical treatments (e.g., acid/base activation) to increase their surface area, pore volume, and functional group density. Watermelon rind was only alkaline-modified in this study, providing only a moderate degree of adsorption enhancement, but not to the same level as dual acid-base modification. It should be noted that the surface area and pore size of an adsorbent have a direct impact on its adsorption capacity. Rice husk and tea waste generally have larger surface areas and microporous structures, which are conducive to dye molecule capture, whereas watermelon rind may have less developed pores.

In addition to being lignocellulosic in nature, watermelon rind is comprised of cellulose, hemicellulose, lignin, and small amounts of pectin, and a large amount of moisture and soluble sugars. These components will likely reduce the material's mechanical properties when wet and may create difficulties maintaining structural integrity during the adsorption process. As such, the ability of watermelon rind to adsorb dye is reduced relative to more rigid and carbon rich materials, such as coffee residue and tea waste.

Although the 78% adsorption efficiency obtained from the alkaline modification of watermelon rind is lower than some of other agricultural waste materials reported in the literature, it is still offers some notable advantages (mild

temperatures, requires no chemical activation, and exhibits consistent Freundlich behaviour suggestive of surface sites capable of chemisorptive interactions with highly reactive EBT conformers) considering it is a non-toxic, abundant, and inexpensive material it operates effectively at. With further optimization—such as acid–base dual modification, surface activation with oxidizing agents, or carbonization—the adsorption efficiency could be markedly improved. Ultimately, this study shows that unoptimized watermelon rind can remove a significant portion of EBT dye, thereby supporting its use as an environmentally friendly biosorbent for the future development of sustainable wastewater treatment technologies.

Table 3: Isotherm constants for the adsorption of *Eriochrome Black T* dye.

	Langmuir		Freudlich
Q_{max}	15.23	K_f	10.56
Rl	0.37	1/n	0.18
R^2	0.97	**R^2**	0.99

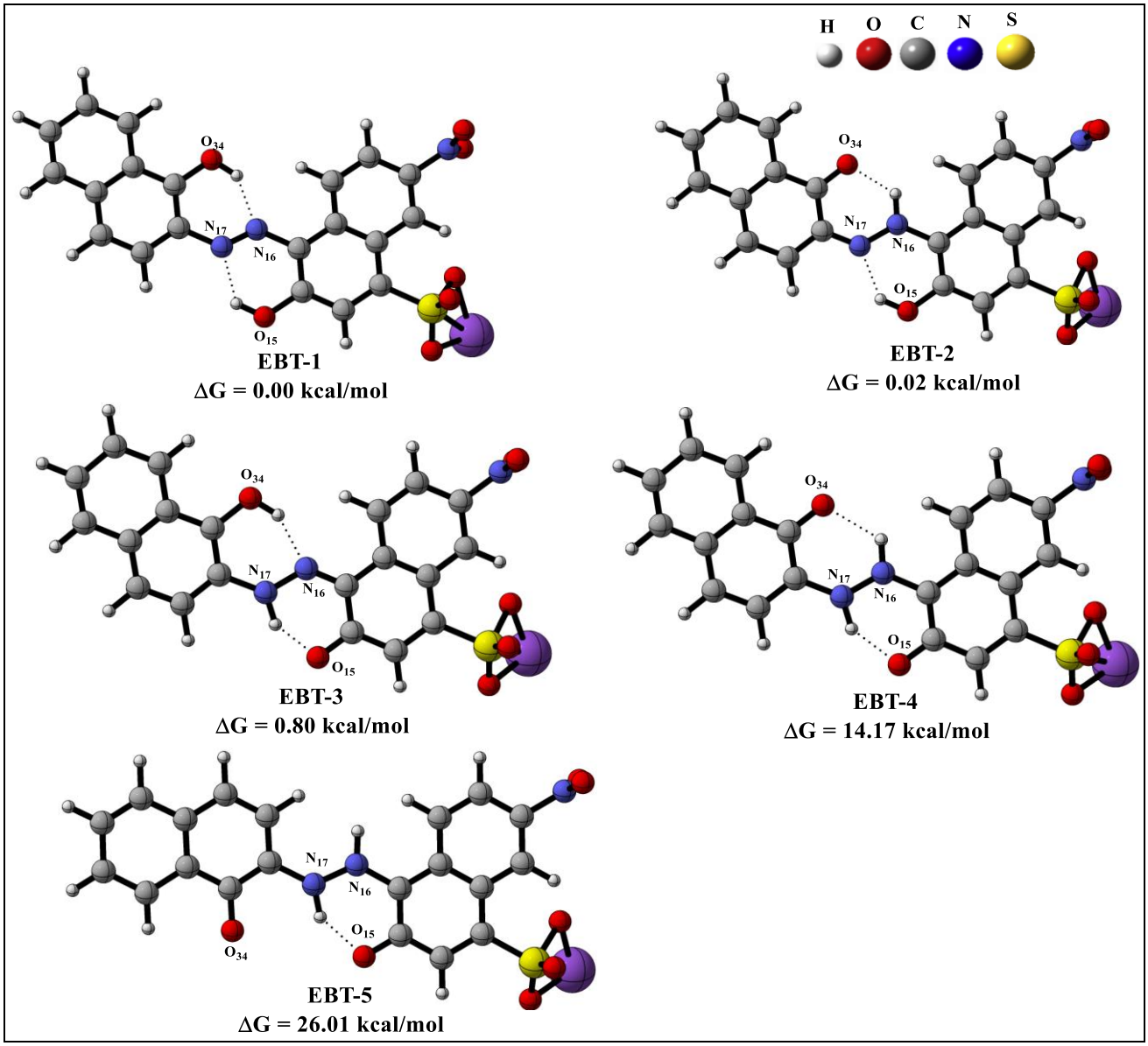

Figure 10: Geometric Structures of the different EBT conformers examined

DFT Calculations

Geometry optimization of different form of the Erichrome Black T Dye

Eriochrome Black T is a hydroxyl-aryl azo dye characterized by several functional groups, including an azo linkage (—N=N—), C—N, C—H, C—S, S=O, N—O, C—O, and O—H bonds, as illustrated in Figure 10. The azo group in EBT connects two aromatic units: naphthalen-1-ol and sodium 3-hydroxy-7-nitronaphthalene-1-sulfonate. To determine the most stable molecular geometry, five conformers (EBT-1 to EBT-5) were analyzed through DFT calculations. In the first conformer, EBT-1, the mo-

Table 4: Comparison of the adsorption capacity of various agricultural wastes as adsorbents for the removal of dyes.

Dye	Adsorbent	Adsorption capacity (%)	References
Deazol Black B EAN, Deafiz Red ME 6BL, and Firstfix Yellow 3RS	Banana peel	93%	(Akter et al., 2021)
Crystal violet	Orange peel	98% (NaOH), 97% (H_2SO_4)	(Pohankar et al., 2025)
Crystal violet (CV) dye	Coconut shell	91%	(Sultana et al., 2022)
Direct Red 23 (DR23) and Direct Red 80 (DR80)	Orange peel	92% and 91% respectively	(Arami et al., 2005)
New Coccine (NCC) azo dye	Modified rice husk	97.3 %	(Tran et al., 2025)
Methylene blue	Banana leaves powder	82%	(Dutta et al., 2025)
Congo red	green coffee residues	78%	(Manzar et al., 2022)
Eriochrome Black T	Nickel modified orange peel	98%	(Kanwal et al., 2025)
Eriochrome Black T	rice hull-based activated carbon	93.14 %	(de Luna et al., 2013)
Eriochrome Black T	Modified rice husk	94 %	(Sudan et al., 2023)
Eriochrome Black T	green coffee residues	≈100%	(Manzar et al., 2022)
Eriochrome Black T	Acid-treated tea waste	95%	(Bansal et al., 2020)
Eriochrome Black T	Watermelon rind	78%	This work

lecule adopts a trans-configuration across the azo linkage, stabilized by dual intramolecular hydrogen bonds between the hydroxyl hydrogens and the azo nitrogen atoms. This structure serves as the reference for evaluating the relative energies of the other conformers. EBT-2 retains the trans-configuration but features a proton transfer from the hydroxyl group of the naphthalen-1-ol moiety to the N16 atom of the azo group. Notably, the Gibbs free energy of EBT-2 is identical to that of EBT-1, suggesting comparable thermodynamic stability. In EBT-3, proton

transfer occurs from the hydroxyl group of the bulkier sodium 3-hydroxy-7-nitronaphthalene-1-sulfonate fragment to N_{17} of the azo group. The relative Gibbs free energy of this conformer is only 0.80 kcal/mol higher than EBT-1, indicating that steric effects from the bulkier fragment are negligible, likely due to the spatial separation of the two aromatic moieties. EBT-4 involves a dual proton transfer from both hydroxyl groups to the azo nitrogens, resulting in a geometry stabilized by two hydrogen bonds between the resulting deprotonated oxygens and the protonated azo nitrogens (Figure 10). However, this conformer exhibits a significantly higher relative Gibbs free energy of 14.17 kcal/mol, indicating that the azo-hydrazone tautomer is energetically unfavorable and unlikely to represent the dominant form of the dye. Lastly, EBT-5 adopts a cis-configuration between the two aromatic fragments. Due to this geometry, only a single hydrogen bond forms between O_{15} and the protonated N_{17}. This conformer has the highest relative Gibbs free energy at 26.01 kcal/mol, effectively ruling it out as a viable geometry for the EBT dye. Throughout all conformers, the sodium ion plays a crucial role in stabilizing the molecular structure, contributing to the overall electronic and conformational stability of the dye.

Focusing on evaluating the bond distances between key atoms involved in the dye's molecular framework across all conformers, Na–O and Na–S bond lengths remained consistent, with minor fluctuations; Na–O ranged from 2.22 to 2.23 Å, while Na–S remained uniformly at 2.68–2.69 Å (Table 5). This minimal variation indicates a stable interaction between the sodium atom and the coordinating oxygen and sulfur atoms across the different forms, suggesting that these atoms form a strong coordination environment. The sulfonic group ($–SO_3^-$) remained structurally invariant among the conformers, with the S–O single bond measuring 1.67 Å and the S=O double bond fixed at 1.40 Å. These consistent values imply that the sulfonic group does not undergo significant geometric alterations between conformers and likely plays a stabilizing role in the overall structure of the dye (Kaur et al., 2021). Similarly, the C–N bond length showed slight variation, with most conformers at 1.47 Å, while EBT-4 and EBT-5 had marginally shorter values of 1.46 Å, possibly due to local structural strain or electronic effects (Nasrallah et al., 2024). A key differentiator among the conformers is observed in the azo and related nitrogen-based functionalities. EBT-1 is the only conformer that retains the characteristic azo (N=N) bond, with a bond length of 1.23 Å, indicative of a strong double bond. In contrast, the other conformers exhibit an N–N single bond (1.40 Å), highlighting tautomeric or structural rearrangements that replace the azo linkage. Additionally, conformers EBT-2 and EBT-3 possess a C=N double bond (1.31 and 1.29 Å, respectively), which is absent in the other structures, further confirming electronic rearrangement or tautomerism in these forms (Table 5). All conformers, except EBT-1, display an N–H bond (1.00 Å), supporting the idea of a proton transfer or hydrogen shift that leads to the loss of azo character (Joshi et al., 2002).

Table 5: Bond lengths of the various EBT conformers examined

Bond Type (Å)	EBT-1	EBT-2	EBT-3	EBT-4	EBT-5
Na-O	2.23	2.22	2.23	2.23	2.23
Na-S	2.69	2.68	2.69	2.69	2.69
S-O	1.67	1.67	1.67	1.67	1.67
S=O	1.40	1.40	1.40	1.40	1.40
C-N	1.47	1.47	1.47	1.46	1.46
N=N	1.23	-	-	-	-
N-N	-	1.40	1.40	1.40	1.40
N=C	-	1.31	1.29	-	-
N-H	-	1.00	1.00	1.00	1.00
N=O	1.20	1.20	1.20	1.20	1.20
C-C	1.40	1.40	1.40	1.40	1.40
C-O	1.43	1.43	1.43	-	-
C=O	-	1.25	1.26	1.27	1.26
C-H	1.07	1.07	1.07	1.07	1.07
O-H	0.96	0.96	0.96	-	-

The nitro group ($–NO_2$) remains intact in all structures, with the N=O bond consistently measured at 1.20 Å, typical for such a strongly electron-withdrawing group. The aromatic C–C bonds maintain uniformity across all conformers (1.40 Å), suggesting that the π-conjugated ring system remains unaffected by conformational changes (Kertesz et al., 2005). Similarly, C–O single bonds are observed in EBT-1 to EBT-3 with a bond length of 1.43 Å, while EBT-4 and EBT-5 show a transition to carbonyl (C=O) groups, evident by shorter bond lengths ranging from 1.25 to 1.27 Å. This shift likely arises from keto-enol tautomerism or oxidation reactions occurring during dye transformation (Rauf et al., 2015). The C–H and O–H bond lengths are consistently recorded at 1.07 Å and 0.96 Å, respectively, in conformers where they appear. Notably, the hydroxyl (O–H) group is absent in EBT-4 and EBT-5, which could be due to intramolecular hydrogen bonding or deprotonation leading to keto formation, as supported by the presence of a C=O bond in these structures (Koll et al., 2006). Geometry optimizations reveal that the EBT dye exhibits rich structural flexibility, with tautomerism, coordination interactions, and electronic rearrangements contributing to the stabilization of multiple conformers. These geometric distinctions are critical for understanding the dye's electronic properties and interaction mechanisms with metal ions or surfaces in analytical and sensor applications.

Natural Bond Orbital (NBO) Analysis and Its Implications for Adsorption Behavior

To gain deeper insight into the electronic properties and potential reactivity of EBT dye relevant to its adsorption on watermelon rind biomass, Natural Bond Orbital (NBO) analysis was conducted for five conformers (EBT-1 to EBT-5). This analysis elucidated key intramolecular donor–acceptor interactions, second-order stabilization energies (E^2), energy gaps between interacting orbitals ($E(j)–E(i)$), and Fock matrix elements ($F(i,j)$) that collectively influence the electronic structure and stability

Table 6: Natural Bond Order (NBO) parameters for EBT conformers

Conformers	Donor (i)	Acceptor (j)	E^2 (kcal/mol)	E(j)-E(i) (a.u)	F(i,j) (a.u)
EBT-1	σ S_{36} -O_{42}	σ* C_{24}-H_{32}	879.68	0.44	0.560
	σ C_{22}-O_{37}	σ* O_{34}-H_{35}	852.49	4.01	1.662
	LP (3) O_{37}	LP* (1) Na_{43}	9.28	0.45	0.061
EBT-2	π N_{38}-O_{40}	σ* S_{35}-O_{36}	733.06	0.46	0.537
	LP (2) O_{40}	σ* N_{16}-H_{44}	590.49	13.57	2.566
	LP (1) O_{15}	σ* C_{27}-C_{29}	363.80	0.42	0.348
EBT-3	LP (1) O_{39}	σ* N_{40}-O_{42}	829.79	0.29	0.440
	σ C_2-S_{37}	σ* C_{20}-O_{35}	801.58	0.37	0.488
	σ C_2-S_{37}	σ* N_{40}-O_{42}	594.73	0.15	0.273
EBT-4	σ C_5-N_{16}	σ* C_{30}-H_{32}	575.05	1.66	0.871
	LP (1) O_{40}	σ* C_{30}-H_{32}	471.39	147.73	7.458
	σ C_2-S_{36}	σ* C_{14}-O_{15}	281.17	0.36	0.320
EBT-5	σ C_1-C_{14}	σ* N_{39}-O_{40}	992.35	8.63	2.625
	LP (1) O_{42}	σ* C_{30}-H_{32}	876.58	2.76	1.424
	LP (1) O_{38}	σ* N_{16}-N_{17}	685.60	2.07	1.066

Table 7: Quantum descriptors for EBT conformers

Parameter	E_{LUMO} (eV)	E_{HOMO} (eV)	ΔE (eV)	EA (eV)	IP (eV)	η (eV)	Σ (eV^{-1})	μ (eV)	χ (eV)	ω (eV)
EBT-1	-2.96	-6.07	3.11	2.96	6.07	1.55	0.64	-4.51	4.51	6.55
EBT-2	-3.36	-5.82	2.46	3.36	5.82	1.23	0.81	-4.59	4.59	8.57
EBT-3	-3.46	-5.87	2.41	3.46	5.87	1.21	0.83	-4.66	4.66	9.01
EBT-4	-3.95	-5.53	1.58	3.95	5.53	0.79	1.26	-4.74	4.74	14.20
EBT-5	-4.06	-5.49	1.43	4.06	5.49	0.71	1.40	-4.77	4.77	15.95

of each conformer (Table 6). In EBT-1, the most significant stabilizing interaction was observed between σ(S36–O42) and σ*(C24–H32) orbitals, with an exceptionally high stabilization energy (E^2) of 879.68 kcal/mol, a small energy gap (0.44 a.u), and a moderate F(i,j) value of 0.560. A comparable interaction involving σ(C22–O37) and σ*(O34–H35) further contributes 852.49 kcal/mol, highlighting strong σ–σ* delocalization pathways that enhance conformational stability. A moderate lone pair interaction between LP(3) O37 and LP*(1) Na43 (E^2 = 9.28 kcal/mol) suggests a weak but relevant coordination to the sodium atom, which could impact dye–metal interactions during adsorption. In EBT-2 delocalization from the π(N38–O40) to σ*(S35–O36) orbitals contributes 733.06 kcal/mol, suggesting efficient resonance along the nitroso-sulfonate backbone. Notably, a strong LP(2) O40 → σ*(N16–H44) interaction (E^2 = 590.49 kcal/mol; F(i,j) = 2.566) underscores the presence of intense hyperconjugative stabilization, potentially affecting the dye's hydrogen-bonding propensity. Additionally, LP(1) O15 → σ*(C27–C29) yields 363.80 kcal/mol, supporting delocalization across the aromatic system, which may enhance π–π interactions during adsorption.

EBT-3 also demonstrates substantial stabilization through lone pair interactions, with LP(1) O39 → σ*(N40–O42) contributing 829.79 kcal/mol. The sulfur center (σ(C2–S37)) participates in multiple interactions with σ*(C20–O35) and σ*(N40–O42), yielding stabilization energies of 801.58 and 594.73 kcal/mol, respectively. These results indicate enhanced electron delocalization along the sulfur–oxygen framework, which may favor adsorption via electrostatic and donor–acceptor interactions. In **EBT-4,** while overall stabilization is lower, notable interactions include σ(C5–N16) → σ*(C30–H32) with 575.05 kcal/mol and LP(1) O40 → σ*(C30–H32) with 471.39 kcal/mol. Although the latter shows an unusually high energy gap (147.73 a.u), the large Fock matrix value (7.458) may indicate a highly strained or potentially transient interaction. This could reflect an unstable or less reactive conformer under adsorption-relevant conditions. The σ(C2–S36) → σ*(C14–O15) delocalization (E^2 = 281.17 kcal/mol) adds to the moderate stabilization profile. **EBT-5** exhibits the strongest donor–acceptor interaction across all conformers, with σ(C1–C14) → σ*(N39–O40) delivering an E^2 of 992.35 kcal/mol and F(i,j) of 2.625, indicating significant electronic stabilization, particularly near the azo or nitro moiety. Additionally, lone pair interactions from O42 and O38 to σ*(C30–H32) and σ*(N16–N17), respectively, contribute 876.58 and 685.60 kcal/mol, suggesting strong hyperconjugative effects that may influence hydrogen bonding and surface affinity.

Therefore, EBT-1 and EBT-5 exhibit the most pronounced stabilizing interactions, suggesting greater electronic stability and possibly enhanced adsorption capabilities. These interactions are largely governed by lone pair → σ* and σ → σ* delocalizations involving electronegative atoms (O, N) and conjugated systems. Such features are critical for EBT"s reactivity, coordination potential with metal ions, and affinity for functional groups on the watermelon rind surface (e.g., hydroxyl, carboxyl, or carbonyl groups). The identified electronic descriptors may thus inform the dye's adsorption efficiency and provide a theoretical foundation for its effective removal in wastewater treatment applications.

Quantum chemical descriptors

To elucidate the electronic structure and reactivity patterns of EBT in the context of its adsorption onto alkaline-modified watermelon rind for dye removal from wastewater, frontier molecular orbital (FMO) analysis was performed. This was complemented by the calculation of key quantum chemical descriptors, namely ionization potential (IP), electron affinity (EA), chemical hardness (η), softness (σ), chemical potential (μ), electronegativity (χ), and electrophilicity index (ω), to further assess the adsorption potential of five EBT conformers (EBT-1 to EBT-5). The HOMO–LUMO plots and calculated descriptors together provide deep insights into the stability and reactivity trends among the EBT conformers (Aihara, 1999; Badeji et al., 2024; Islam & Ghosh, 2011; Zhan et al., 2003).

From the FMO plots in Figure 11, it is evident that the distribution of electron density in the HOMO and LUMO orbitals varies significantly across the conformers, directly influencing their reactivity. In EBT-1, the HOMO is delocalized over the azo and phenolic regions, while the LUMO is concentrated on the sulfonic acid moiety and aromatic ring, suggesting a possibility of intramolecular charge transfer that contributes to its electronic inertness. This conformer also displays the largest energy gap (ΔE = 3.11 eV), confirming its highest chemical stability and lowest reactivity among the five (Aihara, 1999). In contrast, EBT-5, which has the smallest HOMO–LUMO gap (ΔE = 1.43 eV), shows a more significant overlap of HOMO and LUMO densities across conjugated π-systems, particularly around the azo and aromatic regions. This spatial proximity of the orbitals facilitates electron excitation and transfer, indicating enhanced reactivity. This is corroborated by its high electron affinity (EA = 4.06 eV) and low ionization potential (IP = 5.49 eV), both of which imply an enhanced ability to accept and donate electrons, key traits for adsorption interactions (Table 7) (Pal & Chattaraj, 2023). Furthermore, EBT-5 exhibits the lowest chemical hardness (η = 0.71 eV) and the highest softness (σ = 1.40 eV^{-1}), suggesting greater polarizability and a greater propensity to undergo electronic deformation in response to surface interactions. Its high electrophilicity index (ω = 15.95 eV) reflects a strong affinity for nucleophilic species, reinforcing its potential as a highly efficient electron acceptor and an efficient adsorbate in aqueous media.

EBT-4 also shows a low ΔE value (1.58 eV) and similar orbital delocalization across active functional groups, reinforcing its high reactivity and suitability for interactions with adsorbent surfaces. EBT-2 and EBT-3, with intermediate energy gaps (2.46 eV and 2.41 eV, respectively), show HOMO density over the azo and hydroxyl groups, and LUMO distribution on electron-withdrawing moieties, suggesting moderate potential for electron transfer and adsorption. In contrast, EBT-1,with the highest hardness (η = 1.55 eV), lowest softness (σ = 0.64 eV^{-1}), and lowest electrophilicity index (ω = 6.55 eV),is more electronically stable and less reactive, ideal characteristics for applications demanding low reactivity (Pal & Chattaraj, 2023). These properties suggest limited interaction with polar or charged adsorbent surfaces, which makes adsorption-driven removal less favorable.

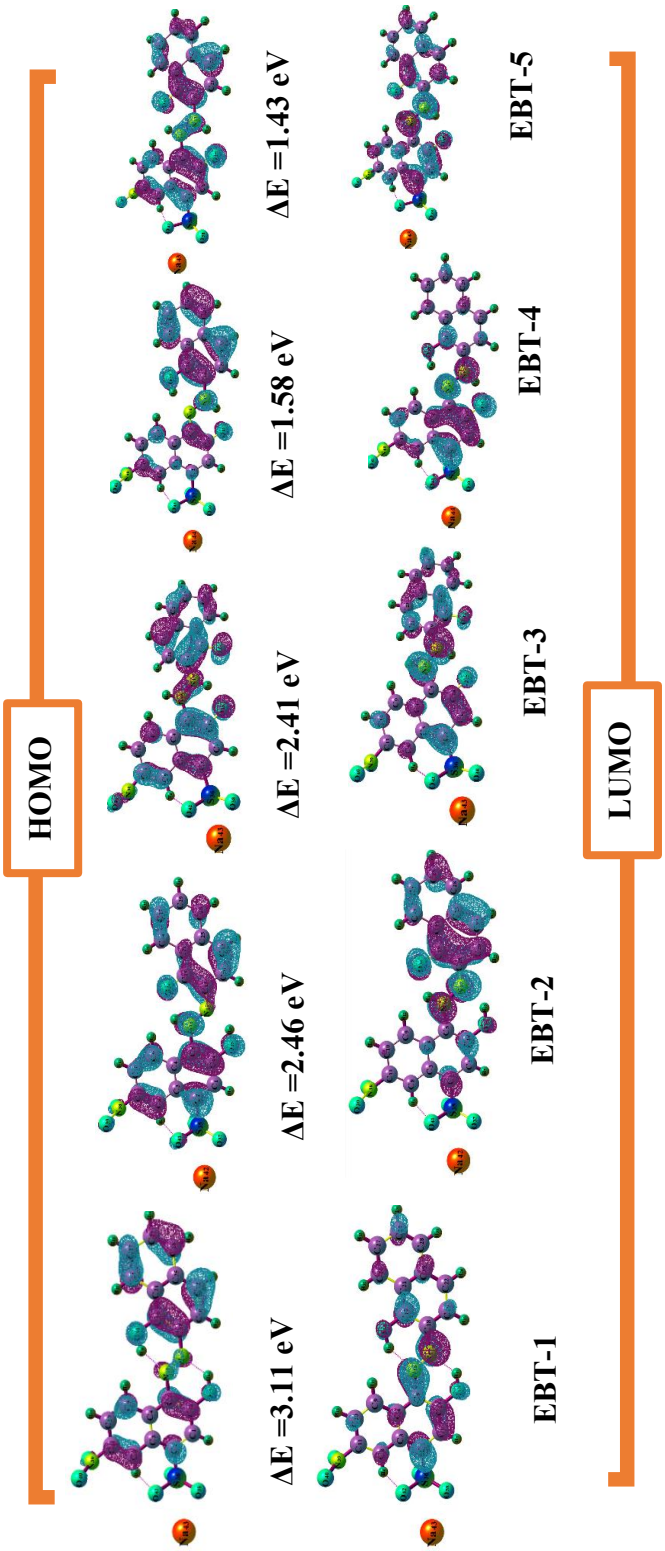

Figure 11: The HOMO-LUMO plots for EBT conformers

While the EBT-4 and EBT-5 conformers exhibit enhanced electron-accepting capacity, extensive orbital delocalization, and a pronounced electrophilic character that favors interactions with the adsorbent, the EBT-1 conformer is notably recalcitrant due to its inherent electronic stability. Consequently, if the dye were

predominantly present in the configurations represented by EBT-4 and EBT-5, its removal from aqueous systems would be significantly more effective, a conclusion that aligns with the findings reported by Mahmood et al. (2021).

Relationship between the quantum descriptors to the experimental thermodynamics

The DFT-based reactivity descriptors showed a good correlation with the experimental thermodynamics in terms of mechanisms. Of the five conformers of EBT, EBT-5 had the smallest HOMO-LUMO gap (ΔE= 1.43eV), lowest hardness (η = 0.71eV), and had the largest electrophilicity (ω= 15.95eV), thus it is the most electronically "soft" and has the greatest ability to receive an electron from a donor site at the adsorbent's surface. This would explain why the dye can easily donate into the LUMO, facilitating charge transfer and orbital overlap, as well as the endothermic (ΔH° = +23.17 kJ/mol) and spontaneous (ΔG° = -2.25 to -6.25 kJ/mol) adsorption behavior observed experimentally. The small ΔE and η indicate that this dye will require relatively little activation energy to be adsorbed onto the adsorbent, whereas the large ω indicates that there should be a strong interaction between the dye and the adsorbent's surface functional groups, consistent with the Freundlich model (R^2 = 0.99, 1/n = 0.18). Therefore, the DFT descriptors support the explanation of the thermodynamic behavior based on a chemisorption mechanism in which donor-acceptor interactions occur between the dye's reactive orbitals and the adsorbent's reactive sites.

Molecular Electrostatic Potential (MESP) Analysis

To complement the electronic structure insights provided by FMO and NBO analyses, the Molecular Electrostatic Potential (MESP) surfaces of the five conformers of EBT were generated and are presented in Figure 12. These surfaces visualize the spatial distribution of electrostatic potential, providing valuable insights into regions prone to electrophilic or nucleophilic interactions. In these maps, red regions denote areas of high electron density (favorable for electrophilic attack), while blue zones highlight electron-deficient areas (susceptible to nucleophilic attack). Intermediate shades (green to yellow) correspond to regions of neutral or weak polarity.

EBT-1 displays a distinct deep blue region near the sodium atom at the molecule's terminal end, suggesting a strongly nucleophilic site capable of interacting with electron-rich or polar functional groups present on the adsorbent surface. Conversely, a vivid red zone is observed around the sulfonic acid group (–SO_3H), particularly concentrated over the oxygen atoms, confirming their electrophilic nature. The molecule exhibits a well-defined bipolar MESP distribution, reflecting a stable dipole moment. This spatial charge separation is consistent with EBT-1's high HOMO–LUMO gap and its pronounced donor–acceptor orbital interactions identified through NBO analysis, indicating chemical stability and moderate reactivity.

In EBT-2, the red lobes over the sulfonyl oxygen atoms remain prominent, reinforcing their role as electrophilic sites. However, the blue region is more broadly distributed than in EBT-1, extending toward the central nitrogen and adjacent amide group (Figure 12). This indicates greater overall polarizability and stronger intramolecular charge separation, as supported by NBO results showing enhanced donor–acceptor delocalization across the sulfonyl and neighboring π systems. The electrostatic profile supports its moderate HOMO–LUMO gap and electrophilicity index, suggesting that EBT-2 could facilitate more dynamic interactions with functional groups such as hydroxyl or carboxyl moieties on the watermelon rind.

EBT-3 shows a less intense blue region centered on the NH and adjacent carbonyl groups, suggesting localized electron-deficient regions. The sulfonic group retains its strong red coloration. Compared to EBT-2, the weaker blue intensity in EBT-3 suggests reduced electrophilic susceptibility. This observation is consistent with its intermediate FMO descriptors and less intense NBO stabilization, suggesting moderate adsorption potential and reactivity.

The MESP surface of EBT-4 exhibits highly localized and intense red regions over the sulfonyl oxygen atoms, along with a deep blue patch on the NH linker. This sharp contrast signifies a highly polarized electronic structure and is in strong agreement with the pronounced donor–acceptor stabilization noted in the NBO analysis, particularly the large hyperconjugative stabilization energy (F(i,j) = 7.458 a.u). The intense MESP contrast supports a higher electrophilicity index, rendering this conformer more chemically reactive and potentially more interactive with polar functional groups on the adsorbent surface.

EBT-5 exhibits the most delocalized and extensive MESP surface among all conformers. Both red and blue regions are spread over larger molecular areas, particularly around the sulfonic, carbonyl, NH, and even aromatic regions. The intense blue patches across the amide and phenyl domains signify multiple nucleophilic sites, while the red zones on the sulfonic group remain consistent. This widespread charge distribution reflects high softness and the strongest electrophilicity index recorded, in agreement with FMO and NBO findings that designate EBT-5 as the most reactive conformer. These features make EBT-5 particularly favorable for multi-point adsorption via electrostatic, hydrogen-bonding, and π–π interactions.

To sum up, the MESP analysis supports the trends observed in the FMO and NBO calculations. EBT-5 is the most reactive conformer, exhibiting significant charge delocalization and multiple reactive sites, which enhance its ability to form electrostatic and hydrogen-bonding interactions with biomass surfaces. Similarly, EBT-4 shows high polarity and localized reactivity, promoting strong interactions with functional groups on alkaline-modified watermelon rind. In contrast, EBT-1 is the most electronically stable conformer, with confined and weak electrostatic features that limit its reactivity and interaction

with adsorbent surfaces, making it more recalcitrant. If EBT-4 or EBT-5 had represented the dominant configuration of the EBT dye, its removal would have been more efficient due to their greater interaction potential. Across all conformers, the sulfonic acid group acts as a key electrophilic site, while NH and carbonyl regions, especially in EBT-4 and EBT-5, serve as nucleophilic zones that facilitate coordination with hydroxyl and carboxyl groups on the adsorbent during dye removal from aqueous media.

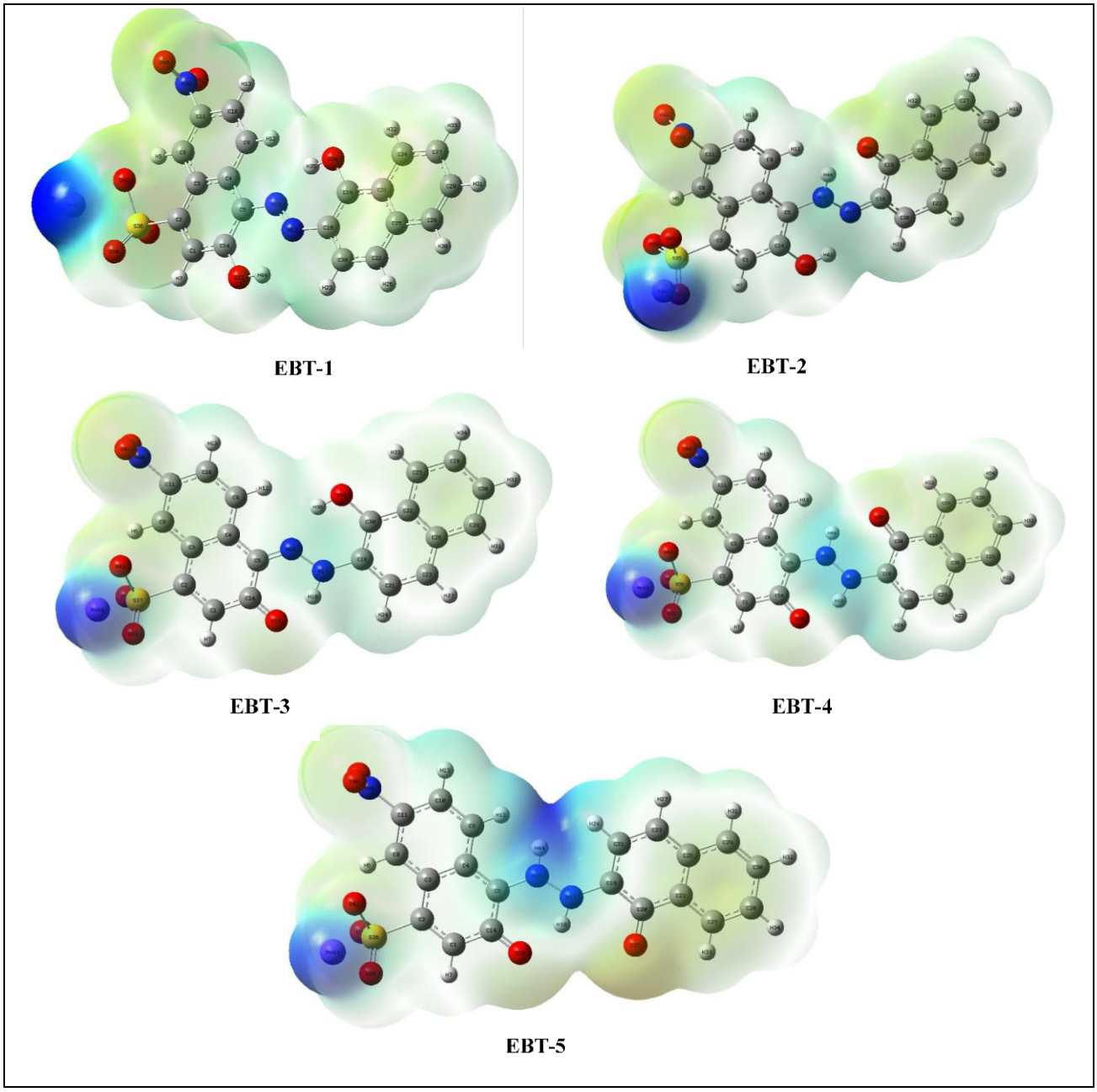

Figure 12: Molecular Electrostatic Potential (MESP) plots for the studied compounds

Mechanistic linkage between DFT results and the adsorption behavior of WR

The quantum chemical results provide mechanistic support for the experimentally observed adsorption behaviour. Among the five EBT conformers, EBT-5 exhibited the lowest HOMO–LUMO energy gap (ΔE = 1.43 eV), implying greater electronic reactivity and a stronger tendency for charge transfer or orbital overlap with the adsorbent surface. This aligns with the Freundlich isotherm fit (Kf = 10.56, 1/n = 0.18, R^2 = 0.99), which signifies a heterogeneous adsorption surface with energetically distinct binding sites. The positive enthalpy ($\Delta H° = +23.17$ kJ mol^{-1}) and entropy ($\Delta S° = +11.63$ kJ mol^{-1} K^{-1}) further support an endothermic, chemisorptive process involving partial electron exchange rather than purely physical interactions. Thus, the DFT-predicted high reactivity of EBT-5 provides a molecular rationale for the experimental evidence of multi-site, energetically diverse adsorption and the increase in spontaneity ($\Delta G° = -2.25$ to -6.25 kJ mol^{-1}) with temperature. The 78% maximum removal efficiency obtained experimentally corroborates this favourable but moderate interaction strength, consistent with partial chemisorption driven by the dye's reactive electronic structure and surface heterogeneity.

The combination of DFT-validated molecular reactivity and favourable thermodynamic parameters thus supports a coherent mechanism in which adsorption proceeds through localized, energetically heterogeneous interactions. Future surface functionalization could exploit EBT-5's low ΔE to further enhance electron-transfer binding and improve adsorption capacity toward the high-performance range reported for contemporary bio-adsorbents.

CONCLUSION

This study confirms the effectiveness of alkali-modified watermelon rind as a sustainable, low-cost adsorbent for removing *Eriochrome Black T* dye from aqueous media. The adsorption achieved a maximum efficiency of 78 %, following the Freundlich isotherm behaviour (R^2 = 0.99, 1/n = 0.18), indicative of heterogeneous surface sites and multilayer adsorption. Thermodynamic parameters (ΔG° = –2.25 to –6.25 kJ/mol; ΔH° = +23.17 kJ/mol) confirm a spontaneous and endothermic process consistent with chemisorption. Kinetic analysis showed that adsorption followed the pseudo-second-order model, highlighting the dominance of surface-controlled mechanisms. DFT, NBO, and FMO analyses further elucidated that the EBT-5 conformer (ΔE = 1.43 eV) exhibits the highest reactivity, explaining the experimentally observed affinity for heterogeneous sites. Therefore, integrating experimental and quantum-chemical insights provides a coherent mechanistic understanding of dye–adsorbent interactions and validates the potential of agricultural residues as effective biosorbents. These findings position alkali-modified watermelon rind as a readily available green adsorbent for industrial wastewater treatment, with DFT guidance offering a rational pathway for future surface modifications and scalability.

REFERENCES

Aihara, J. (1999). Reduced HOMO−LUMO gap as an index of kinetic stability for polycyclic aromatic hydrocarbons. *The Journal of Physical Chemistry A, 103*(37), 7487–7495. [Crossref]

Akinyemi, O. P., Akinbomi, J. G., & Abbey, D. M. (2020). Comparative characterization of plantain peel, pawpaw peel and watermelon rind using FTIR. *Engineering and Technology Research Journal, 5*(1), 1–6. [Crossref]

Akter, M., Rahman, F. B. A., Abedin, M. Z., & Kabir, S. F. (2021). Adsorption characteristics of banana peel in the removal of dyes from textile effluent. *Textiles, 1*(2), 361–375. [Crossref]

Al-Degs, Y. S., El-Barghouthi, M. I., El-Sheikh, A. H., & Walker, G. M. (2008). Effect of solution pH, ionic strength, and temperature on adsorption behavior of reactive dyes on activated carbon. *Dyes and Pigments, 77*(1), 16–23. [Crossref]

Anadebe, V. C., Lgaz, H., Aldalbahi, A., Lee, H., Mathias, G. E., Badeji, A. A., Thakur, A., & Ebenso, E. E. (2025). Interfacial inhibition of mild steel corrosion by Abemaciclib and Abrocitinib in acidic media: Insights from density functional theory and molecular dynamics simulations. *ChemistrySelect, 10*(32), e03502. [Crossref]

Andersson, M. P., & Uvdal, P. (2005). New scale factors for harmonic vibrational frequencies using the B3LYP density functional method with the triple-ζ basis set 6-311+G(d,p). *The Journal of Physical Chemistry A, 109*(12), 2937–2941. [Crossref]

Andrienko, G. (2010). *Chemcraft—Graphical software for visualization of quantum chemistry computations.* [Link]

Afolalu, S. A., Ikumapayi, O. M., Ogedengbe, T. S., & Ogundipe, A. T. (2022). Techniques of agro wastes materials as viable adsorbents—A review. In *Proceedings of the International Conference on Industrial Engineering and Operations Management* (Vol. 5, No. 7). Nsukka, Nigeria. [Crossref]

Arami, M., Limaee, N. Y., Mahmoodi, N. M., & Tabrizi, N. S. (2005). Removal of dyes from colored textile wastewater by orange peel adsorbent: Equilibrium and kinetic studies. *Journal of Colloid and Interface Science, 288*(2), 371–376. [Crossref]

Badeji, A. A., Omoniyi, M. T., Ogunbayo, T. B., Oladipo, S. D., & Akinbulu, I. A. (2024). Quantum chemical investigation of the degradation of acid orange 7 by different oxidants. *Discover Chemistry, 1*(1), 55. [Crossref]

Bansal, M., Patnala, P. K., & Dugmore, T. (2020). Adsorption of Eriochrome Black-T (EBT) using tea waste as a low cost adsorbent by batch studies: A green approach for dye effluent treatments. *Current Research in Green and Sustainable Chemistry, 3*, 100036. [Crossref]

Becke, A. D. (1993). A new mixing of Hartree–Fock and local density-functional theories. *The Journal of Chemical Physics, 98*(2), 1372–1377. [Crossref]

Beegum, P. P., Sagar, V. R., Kar, A., Varghese, E., Singh, S., & Pongener, A. (2024). Optimization of pectin extraction from watermelon rind and characterization of the extracted pectin. *Journal of Agricultural Engineering, 61*(6), 862–875. [Crossref]

de Luna, M. D. G., Flores, E. D., Genuino, D. A. D., Futalan, C. M., & Wan, M.-W. (2013). Adsorption of Eriochrome Black T (EBT) dye using activated carbon prepared from waste rice hulls—Optimization, isotherm and kinetic studies. *Journal of the Taiwan Institute of Chemical Engineers, 44*(4), 646–653. [Crossref]

Dennington, R., Keith, T. A., & Millam, J. M. (2016). *GaussView* (Version 6.0.16) [Computer software]. Semichem Inc.

Dutta, S., Jahan, M., Kaur, N., Barna, S., Sathi, N., Sultana, R., Dhar, P., Al Mamun, M., Chakrabarty, S., & Amin, M. (2025). Banana leaves powder as an effective, low-cost adsorbent for methyl blue dye removal: Kinetics, isothermal, thermodynamics, ANN and DFT analysis. *International Journal of Environmental Science and Technology, 22*(3), 1865–1890. [Crossref]

Foster, C. N. (2015). *Agricultural wastes: Characteristics, types, and management*. Nova Science Publishers.

Freundlich, H. (1906). Adsorption in solids. *Zeitschrift für Physikalische Chemie, 57*, 385–470. [Crossref]

Frisch, M. J., Trucks, G. W., Schlegel, H. B., Scuseria, G. E., Robb, M. A., Cheeseman, J. R., Scalmani, G., Barone, V., Petersson, G. A., & Nakatsuji, H. (2016). *Gaussian 16* (Revision C.01) [Computer software]. Gaussian, Inc.

Fujimoto, N., Sawada, T., Tada, E., & Nishikata, A. (2017). Effect of pH on hydrogen absorption into steel in neutral and alkaline solutions. *Materials Transactions, 58*(2), 211–217. [Crossref]

Grandhi, R. (1993). Structural optimization with frequency constraints—A review. *AIAA Journal, 31*(12), 2296–2303. [Crossref]

Harrache, Z., & Abbas, M. (2022). Elimination of a cationic dye in aqueous solution by adsorption on activated carbon: Optimization of analytical parameters, modeling and thermodynamic study. *Journal of Engineered Fibers and Fabrics, 17*. [Crossref]

Hassan, H. B. (2014). Density function theory B3LYP/6-31G calculation of geometry optimization and energies of donor-bridge-acceptor molecular system. *International Journal of Current Engineering and Technology, 4*, 2342–2345.

Ho, Y. S., & McKay, G. (1999). Pseudo-second order model for sorption processes. *Process Biochemistry, 34*(5), 451–465. [Crossref]

Huang, Y., Rong, C., Zhang, R., & Liu, S. (2017). Evaluating frontier orbital energy and HOMO/LUMO gap with descriptors from density functional reactivity theory. *Journal of Molecular Modeling, 23*(1), 3. [Crossref]

Islam, N., & Ghosh, D. C. (2011). The electronegativity and the global hardness are periodic properties of atoms. *Journal of Quantum Information Science, 1*(3), 135–141. [Crossref]

Johnson, T. A., Jain, N., Joshi, H., & Prasad, S. (2008). Agricultural and agro-processing wastes as low cost adsorbents for metal removal from wastewater: A review. *Journal of Scientific and Industrial Research, 67*(9), 647–658.

Joshi, H., Kamounah, F. S., Gooijer, C., van der Zwan, G., & Antonov, L. (2002). Excited state intramolecular proton transfer in some tautomeric azo dyes and schiff bases containing an intramolecular hydrogen bond. *Journal of Photochemistry and Photobiology A: Chemistry, 152*(1–3), 183–191. [Crossref]

Kanwal, A., Abid, J., Gul, S., Nouman, M., Idris, A. M., & Ullah, H. (2025). Nickel-modified orange peel biochar for the efficient adsorptive removal of Eriochrome black T from aqueous solution. *Water, 17*(10), 1484. [Crossref]

Kaur, Y., Jasrotia, T., Kumar, R., Chaudhary, G. R., & Chaudhary, S. (2021). Adsorptive removal of Eriochrome black T (EBT) dye by using surface active low cost zinc oxide nanoparticles: A comparative overview. *Chemosphere, 278*, 130366. [Crossref]

Kertesz, M., Choi, C. H., & Yang, S. (2005). Conjugated polymers and aromaticity. *Chemical Reviews, 105*(10), 3448–3481. [Crossref]

Kishor, R., Purchase, D., Ferreira, L. F. R., Mulla, S. I., Bilal, M., & Bharagava, R. N. (2020). Environmental and health hazards of textile industry wastewater pollutants and its treatment approaches. In C. M. Hussain (Ed.), *Handbook of environmental materials management* (pp. 1–24). Springer. [Crossref]

Kishor, R., Purchase, D., Saratale, G. D., Saratale, R. G., Ferreira, L. F. R., Bilal, M., Chandra, R., & Bharagava, R. N. (2021). Ecotoxicological and health concerns of persistent coloring pollutants of textile industry wastewater and treatment approaches for environmental safety. *Journal of Environmental Chemical Engineering, 9*(2), 105012. [Crossref]

Koll, A., Karpfen, A., & Wolschann, P. (2006). Structural and energetic consequences of the formation of intramolecular hydrogen bonds. *Journal of Molecular Structure, 790*(1–3), 55–64. [Crossref]

Lagergren, S. (1898). About the theory of so-called adsorption of soluble substances. *Kungliga Svenska Vetenskapsakademiens Handlingar, 24*(4), 1–39.

Langmuir, I. (1918). The adsorption of gases on plane surfaces of glass, mica and platinum. *Journal of the American Chemical Society, 40*(9), 1361–1403. [Crossref]

Legault, C. Y. (2016). *CYLview* (Version 1.0b) [Computer software]. Université de Sherbrooke. [Link]

Lellis, B., Fávaro-Polonio, C. Z., Pamphile, J. A., & Polonio, J. C. (2019). Effects of textile dyes on health and the environment and bioremediation potential of living organisms. *Biotechnology Research and Innovation, 3*(2), 275–290. [Crossref]

Liu, Y., Biswas, B., Hassan, M., & Naidu, R. (2024). Green adsorbents for environmental remediation: Synthesis methods, ecotoxicity, and reusability prospects. *Processes, 12*(6), 1195. [Crossref]

Mahmood, R. (2021). The uptake of Eriochrome Black T dye from wastewater utilizing synthetized cadmium sulfide nanoparticles. *Egyptian Journal of Chemistry, 64*(12), 7323–7333. [Crossref]

Mahmoodi, N. M. (2011). Equilibrium, kinetics, and thermodynamics of dye removal using alginate in binary systems. *Journal of Chemical & Engineering Data, 56*(6), 2802–2811. [Crossref]

Manzar, M. S., Zubair, M., Khan, N. A., Husain Khan, A., Baig, U., Aziz, M. A., Blaisi, N. I., & Abdel-Magid, H. I. (2022). Adsorption behaviour of green coffee residues for decolourization of hazardous Congo red and Eriochrome Black T dyes from aqueous solutions. *International Journal of Environmental Analytical Chemistry, 102*(18), 6405–6421. [Crossref]

Nasrallah, D. A., AlAbdulaal, T., Zahran, H., Yahia, I., & Mohammed, M. (2024). Investigation of linear and nonlinear optical characterization of triple

blended polymers incorporated with varying content of Eriochrome Black T dye for low-cost optical technologies and limiting absorption. *Materials Science in Semiconductor Processing, 175*, 108179. [Crossref]

Okieimen, F., Okiemen, C., & Wuana, R. (2007). Preparation and characterization of activated carbon from rice husks. *Journal of the Chemical Society of Nigeria, 32*, 126–136.

Ogunlana, A. A., Zou, J., & Bao, X. (2018). Computational insights into the mechanisms of Ru-catalyzed cycloisomerization of 2-ethynylaniline and 2-(2-propynyl)tosylanilide: The role of pyridine in assisting the metal-vinylidene formation. *Journal of Organometallic Chemistry, 864*, 160–168. [Crossref]

Olukanni, D. O., & Mnenga, M. U. (2015). Municipal solid waste generation and characterization: A case study of Ota, Nigeria. *International Journal of Environmental Science and Toxicology Research, 3*(1), 1–8.

Onyango, C., Nyairo, W., Tchieta, G. P., & Shikuku, V. O. (2025). Watermelon rind based adsorbents for the removal of water pollutants: A critical review. *Frontiers in Environmental Chemistry, 6*, 1568695. [Crossref]

Othman, N., Azhar, N., Megat Abdul Rani, P. S., & Mohamed Zaini, H. (2016). Metal removal and antimicrobial properties of watermelon rind modified with clove. *MATEC Web of Conferences, 78*, 01028. [Crossref]

Padhi, B. (2012). Pollution due to synthetic dyes toxicity & carcinogenicity studies and remediation. *International Journal of Environmental Sciences, 3*(3), 940–955.

Pal, R., & Chattaraj, P. K. (2023). Electrophilicity index revisited. *Journal of Computational Chemistry, 44*(3), 278–297. [Crossref]

Pohankar, P., Sharma, Y., Manikandan, A., & Blaise, D. (2025). Adsorption of crystal violet dye from waste water by using orange peel (citrus sinensis) as an eco-friendly adsorbent. *Plant Archives, 25*(1), 2492–2497. [Crossref]

Priyan, V. V., Sathasivam, J., Kumar, A., & Narayanasamy, S. (2024). Valorisation of agricultural waste into a low-cost adsorbent: Perspective of reutilization. In R. Neelancherry, B. Gao, & A. Wisniewski Jr (Eds.), *Agricultural waste to value-added products* (pp. 125–149). Springer. [Crossref]

Rauf, M., Hisaindee, S., & Saleh, N. (2015). Spectroscopic studies of keto-enol tautomeric equilibrium of azo dyes. *RSC Advances, 5*(23), 18097–18110. [Crossref]

Rekha Krishnan, G., Prabhakaran, K., & George, B. K. (2023). Watermelon rind derived carbon monolith as potential regenerable adsorbent for perchlorate. *Bioresource Technology Reports, 21*, 101361. [Crossref]

Said, K. A. M., Ismail, A. F., Karim, Z. A., Abdullah, M. S., & Hafeez, A. (2021). A review of technologies for the phenolic compounds recovery and phenol removal from wastewater. *Process Safety and Environmental Protection, 151*, 257–289. [Crossref]

Shukla, S., Khan, R., Srivastava, M. M., & Zahmatkesh, S. (2024). Valorization of waste watermelon rinds as a bio-adsorbent for efficient removal of methylene blue dye from aqueous solutions. *Applied Biochemistry and Biotechnology, 196*(5), 2534–2548. [Crossref]

Sudan, S., Khajuria, A., & Kaushal, J. (2023). Adsorption potential of pristine biochar synthesized from rice husk waste for the removal of Eriochrome Black azo dye. *Materials Today: Proceedings*. [Crossref]

Sultana, S., Islam, K., Hasan, M. A., Khan, H. J., Khan, M. A. R., Deb, A., Al Raihan, M., & Rahman, M. W. (2022). Adsorption of crystal violet dye by coconut husk powder: Isotherm, kinetics and thermodynamics perspectives. *Environmental Nanotechnology, Monitoring & Management, 17*, 100651. [Crossref]

Suresh, C. H., Remya, G. S., & Anjalikrishna, P. K. (2022). Molecular electrostatic potential analysis: A powerful tool to interpret and predict chemical reactivity. *WIREs Computational Molecular Science, 12*(5), e1601. [Crossref]

Thakur, S., & Chauhan, M. S. (2018). Treatment of dye wastewater from textile industry by electrocoagulation and Fenton oxidation: A review. In V. P. Singh, S. Yadav, & R. N. Yadava (Eds.), *Water quality management* (pp. 117–129). Springer. [Crossref]

Tran, T. K. C., Truong, T. T. T., Le, A. L., Do, D. A. M., Nguyen, T. G., Tran, T. D., & Pham, T. D. (2025). Synthesis, characterization of novel protein-modified rice husk biochar and their applications for highly adsorptive removal azo dye in water. *Environmental Technology & Innovation, 37*, 104037. [Crossref]

Vigdorowitsch, M., Pchelintsev, A., Tsygankova, L., & Tanygina, E. (2021). Freundlich isotherm: An adsorption model complete framework. *Applied Sciences, 11*(17), 8078. [Crossref]

Vlahović, M., Vušović, N., Vlahović, M., Mihajlović, S., & Žarković, D. (2024). Optimizing textile effluents treatment: From conventional to cutting-edge solutions. *Tekstilna Industrija, 72*(3), 46–58. [Crossref]

Wang, Q., Wang, Y., Yuan, L., Zou, T., Zhang, W., Zhang, X., Zhang, L., & Huang, X. (2022). Utilization of low-cost watermelon rind for efficient removal of Cd (II) from aqueous solutions: Adsorption performance and mechanism elucidation. *Chemical Engineering Journal Advances, 12*, 100393. [Crossref]

Yaseen, D. A., & Scholz, M. (2019). Textile dye wastewater characteristics and constituents of synthetic effluents: A critical review. *International Journal of Environmental Science and Technology, 16*(2), 1193–1226. [Crossref]

Zhan, C.-G., Nichols, J. A., & Dixon, D. A. (2003). Ionization potential, electron affinity, electronegativity, hardness, and electron

excitation energy: Molecular properties from density functional theory orbital energies. *The Journal of Physical Chemistry A, 107*(20), 4184–4195. [Crossref]

The TOC figure illustrating watermelon rind valorization pathway is given below